The Astrophysical Journal, 749:122 (12pp), 2012 April 20 doi:10.1088/0004-637X/749/2/122


# SGR J1550−5418 BURSTS DETECTED WITH THE *FERMI* GAMMA-RAY BURST MONITOR DURING ITS MOST PROLIFIC ACTIVITY

A. J. van der Horst[1,2], C. Kouveliotou[3], N. M. Gorgone[4], Y. Kaneko[5], M. G. Baring[6], S. Guiriec[7,8], E. Göğüş[5], J. Granot[9,10,11], A. L. Watts[2], L. Lin[5,7,12], P. N. Bhat[7], E. Bissaldi[13], V. L. Chaplin[7], M. H. Finger[1], N. Gehrels[8], M. H. Gibby[14], M. M. Giles[14], A. Goldstein[7], D. Gruber[13], A. K. Harding[8], L. Kaper[2], A. von Kienlin[13], M. van der Klis[2], S. McBreen[15], J. Mcenery[8], C. A. Meegan[1], W. S. Paciesas[7], A. Pe'er[16], R. D. Preece[7], E. Ramirez-Ruiz[17], A. Rau[13], S. Wachter[18], C. Wilson-Hodge[3], P. M. Woods[19], and R. A. M. J. Wijers[2]

[1] Universities Space Research Association, NSSTC, Huntsville, AL 35805, USA
[2] Astronomical Institute "Anton Pannekoek," University of Amsterdam, Postbus 94249, 1090 GE Amsterdam, The Netherlands; A.J.VanDerHorst@uva.nl
[3] Space Science Office, VP62, NASA/Marshall Space Flight Center, Huntsville, AL 35812, USA
[4] Connecticut College, New London, CT 06320, USA
[5] Sabancı University, Orhanlı-Tuzla, İstanbul 34956, Turkey
[6] Department of Physics and Astronomy, Rice University, MS-108, P.O. Box 1892, Houston, TX 77251, USA
[7] University of Alabama, Huntsville, CSPAR, Huntsville, AL 35805, USA
[8] NASA Goddard Space Flight Center, Greenbelt, MD 20771, USA
[9] Racah Institute of Physics, The Hebrew University, Jerusalem 91904, Israel
[10] Raymond and Beverly Sackler School of Physics & Astronomy, Tel Aviv University, Tel Aviv 69978, Israel
[11] Centre for Astrophysics Research, University of Hertfordshire, College Lane, Hatfield, AL10 9AB, UK
[12] National Astronomical Observatories, Chinese Academy of Sciences, Beijing 100012, China
[13] Max Planck Institute for Extraterrestrial Physics, Giessenbachstrasse, Postfach 1312, 85748 Garching, Germany
[14] Jacobs Technology, Inc., Huntsville, AL, USA
[15] University College, Dublin, Belfield, Stillorgan Road, Dublin 4, Ireland
[16] Harvard-Smithsonian Center for Astrophysics, Cambridge, MA 02138, USA
[17] Department of Astronomy and Astrophysics, University of California, Santa Cruz, CA 95064, USA
[18] IPAC, California Institute of Technology, 1200 E. California Blvd., MS 220-6, Pasadena, CA 91125, USA
[19] Corvid Technologies, 689 Discovery Drive, Huntsville, AL 35806, USA
*Received 2011 September 20; accepted 2012 February 11; published 2012 March 29*

## ABSTRACT

We have performed detailed temporal and time-integrated spectral analysis of 286 bursts from SGR J1550−5418 detected with the *Fermi* Gamma-ray Burst Monitor (GBM) in 2009 January, resulting in the largest uniform sample of temporal and spectral properties of SGR J1550−5418 bursts. We have used the combination of broadband and high time-resolution data provided with GBM to perform statistical studies for the source properties. We determine the durations, emission times, duty cycles, and rise times for all bursts, and find that they are typical of SGR bursts. We explore various models in our spectral analysis, and conclude that the spectra of SGR J1550−5418 bursts in the 8–200 keV band are equally well described by optically thin thermal bremsstrahlung (OTTB), a power law (PL) with an exponential cutoff (Comptonized model), and two blackbody (BB) functions (BB+BB). In the spectral fits with the Comptonized model, we find a mean PL index of −0.92, close to the OTTB index of −1. We show that there is an anti-correlation between the Comptonized $E_{\rm peak}$ and the burst fluence and average flux. For the BB+BB fits, we find that the fluences and emission areas of the two *BB* functions are correlated. The low-temperature BB has an emission area comparable to the neutron star surface area, independent of the temperature, while the high-temperature BB has a much smaller area and shows an anti-correlation between emission area and temperature. We compare the properties of these bursts with bursts observed from other SGR sources during extreme activations, and discuss the implications of our results in the context of magnetar burst models.

*Key words:* pulsars: individual (SGR J1550−5418, 1E 1547.0−5408, PSR J1550−5418) – stars: neutron – X-rays: bursts

## 1. INTRODUCTION

Magnetars are members of the diverse neutron star family: they are isolated neutron stars whose persistent X-ray emission and soft gamma-ray bursts are powered by their extremely strong magnetic fields of $10^{14}$–$10^{15}$ G (Duncan & Thompson 1992; Kouveliotou et al. 1998; Thompson et al. 2002). Historically, two classes of sources have been identified with characteristics that could be explained by the magnetar model: anomalous X-ray pulsars (AXPs) and soft gamma repeaters (SGRs). These original classifications were based on several distinct differences between the two populations (for reviews, see Woods & Thompson 2006; Mereghetti 2008), but it has now become clear that they share several properties. Therefore, AXPs and SGRs form one source class with small differences still maintained, most notably the rates and energetics of bursts during active episodes, with the luminosity distributions of AXP bursts being lower by orders of magnitude than those of SGR bursts.

The source discussed in this paper was discovered by the *Einstein* X-ray satellite and named 1E 1547.0−5408 (Lamb & Markert 1981); it was subsequently confirmed in the *ASCA* Galactic plane survey (Sugizaki et al. 2001). *Chandra* and *XMM-Newton* observations identified the source as a magnetar candidate based on its varying X-ray flux, spectral characteristics, and the tentative association with the supernova remnant G 327.24-0.13 (Gelfand & Gaensler 2007), although no X-ray pulsations or soft gamma-ray bursts were detected. The

magnetar nature of the source was confirmed by the discovery of radio pulsations with the Parkes radio telescope, which were subsequently associated with 1E 1547.0−5408 with ATCA observations; the radio source was named PSR J1550−5418 (Camilo et al. 2007). It is one of only three magnetars exhibiting pulsed radio emission, the other ones being XTE J1810−197 (Camilo et al. 2006) and PSR J1622−4950 (Levin et al. 2010). A surface dipole magnetic field strength of $2.2 \times 10^{14}$ G has been inferred from its spin period of 2.07 s (the shortest of all magnetars) and its period derivative of $2.32 \times 10^{-11}$ s s$^{-1}$. Further studies of the radio and persistent X-ray emission showed that the rotation and magnetic axes of this neutron star are nearly aligned (Halpern et al. 2008; Camilo et al. 2008).

Given its characteristics and the lack of bursting behavior, the magnetar source was originally classified as an AXP (Camilo et al. 2007). However, in 2008 the source started a series of three active episodes that covered over half a year: the first was in 2008 October; the second, most burst active one started in 2009 January; and the last in 2009 March. During the first episode, the *Swift* Burst Alert Telescope (BAT; Krimm et al. 2008a, 2008b; Israel et al. 2010) and the *Fermi* Gamma-ray Burst Monitor (GBM; von Kienlin & Briggs 2008; van der Horst & Briggs 2008) detected several tens of bursts; as a result the source was reclassified as an SGR and designated SGR J1550−5418. This reclassification was firmly established by the extreme bursting activity displayed on 2009 January 22, when hundreds of bursts were detected in one day by several instruments, i.e., *Swift* (Gronwall et al. 2009; Scholz & Kaspi 2011), *Fermi*/GBM (Connaughton & Briggs 2009; von Kienlin & Connaughton 2009), *INTEGRAL*/SPI-ACS (Savchenko et al. 2009; Mereghetti et al. 2009a, 2009b) and IBIS/ISGRI (Savchenko et al. 2010), *Suzaku* WAM (Terada et al. 2009), RHESSI (Bellm et al. 2009), and KONUS-*WIND* (Golenetskii et al. 2009a, 2009b, 2009c). These bursts had durations and luminosities typical of SGR bursts; in fact some were so bright that they caused ionospheric disturbances observed in very low frequency radio wave data (Chakrabarti et al. 2009; Tanaka et al. 2010).

The distance to the source is currently uncertain, varying from ∼9 kpc, based on the radio dispersion measure (Camilo et al. 2007), down to ∼4–5 kpc, based on the tentative supernova remnant association (Gelfand & Gaensler 2007) and the detection of expanding dust-scattering X-ray rings (Tiengo et al. 2010). The former estimate has large uncertainties arising from the Galactic free electron density model of Cordes & Lazio (2002) used for calculating the radio dispersion measure. Therefore, we adopt here a source distance of 5 kpc. Throughout this paper we use the notation $d_5 = \text{distance}/(5\,\text{kpc})$, when calculating burst energies and luminosities.

In this paper, we present the temporal and time-integrated spectral analysis of 286 SGR J1550−5418 bursts detected with GBM in 2009 January for which we have high time-resolution data. Given the very large field of view (the entire unocculted sky) of GBM, this is the largest uniform sample of temporal and spectral properties of SGR J1550−5418 bursts during the January activation. This data set enables us to determine their durations, spectral shapes, and energetics, and compare them with other magnetar sources during similar high bursting activity periods: SGR 1900+14 (Göğüş et al. 1999; Israel et al. 2008), SGR 1806−20 (Göğüş et al. 2000), AXP 1E 2259+586 (Gavriil et al. 2004), and SGR 1627−41 (Esposito et al. 2008). We also compare our results with the analysis of bursts detected by *Swift* during the same time period (Scholz & Kaspi 2011), and discuss them in the framework of current theoretical models. Here, we focus on the 2009 January bursts, while the analysis of the 2008 October and 2009 February–March bursts are discussed in von Kienlin et al. (2012, in preparation) and Younes et al. (2012, in preparation). The discovery of enhanced persistent emission in the GBM data during the beginning of activity on January 22 has been presented in Kaneko et al. (2010).

In Section 2 we present our data selection of GBM bursts, and in Sections 3 and 4 we present our temporal and spectral analysis, respectively. We discuss our results and their interpretation in the context of other bursting magnetar sources in Section 5, and we summarize in Section 6.

## 2. SAMPLE AND DATA SELECTION

GBM comprises 14 detectors with a field of view of 8 sr (the entire sky unocculted by the Earth): 12 NaI detectors covering a spectral range from 8 keV to 1 MeV, and two BGO detectors covering 0.2–40 MeV (see Meegan et al. 2009 for an overview of the instrument and its capabilities). We use here only data from the NaI detectors because SGR bursts are not detected above 200 keV.

GBM collects three data types: time-tagged event (TTE), CTIME and CSPEC (Meegan et al. 2009). To perform detailed temporal and spectral analyses over the typical burst durations of ∼0.1 s, we selected for our sample only events with TTE data, which provide a time-tagged photon event list with a temporal resolution as low as 2 $\mu$s in 128 energy channels logarithmically spaced over the energy range of the NaI detectors. The other two data types cannot be used for our purposes, because either their accumulation times are much longer (CSPEC) or they have a worse spectral resolution (CTIME). The TTE data type covers the time range from 30 s prior to 300 s after a trigger, and GBM has been designed to not trigger for 600 s after a previous trigger. This leaves at least 270 s between consecutive triggers without TTE data. Fortuitously, SGR J1550−5418 triggered GBM very frequently (41 times on January 22 alone), providing a good TTE data coverage for hundreds of bursts.

To perform a comprehensive and systematic study of the SGR J1550−5418 bursts, we applied our untriggered burst search algorithm to the CTIME data type in both continuous (0.256 s time resolution) and trigger (0.064 s time resolution) modes (Kaneko et al. 2010). For each burst, we required a count rate above background in the 10–50 keV energy range of at least $5.5\sigma$ and $4.5\sigma$ in the first and second brightest detectors, respectively. Note that the GBM trigger criteria differ from the ones applied in our untriggered burst search, resulting in omitting several GBM triggers from our sample. We then compared each burst candidate light curve and spectral behavior to those of typical SGR bursts, and checked if the SGR J1550−5418 location was consistent with the relative rates in the NaI detectors at the time of the burst (for the orientation of the spacecraft at that time). The untriggered burst search resulted in 555 events on January 22 alone and 597 events in total up to January 29. This total number, however, includes events for which TTE data are not available and thus excluded from this analysis. Moreover, in several occasions multiple events were part of the same burst as defined by the method employed by Göğüş et al. (2001). More specifically, we required that for two events to qualify as two separate bursts, the time between their peaks in the TTE data had to be greater than a quarter of the spin period of the SGR (0.5 s in the case of SGR J1550−5418), and the count rate level had to drop to the background level between

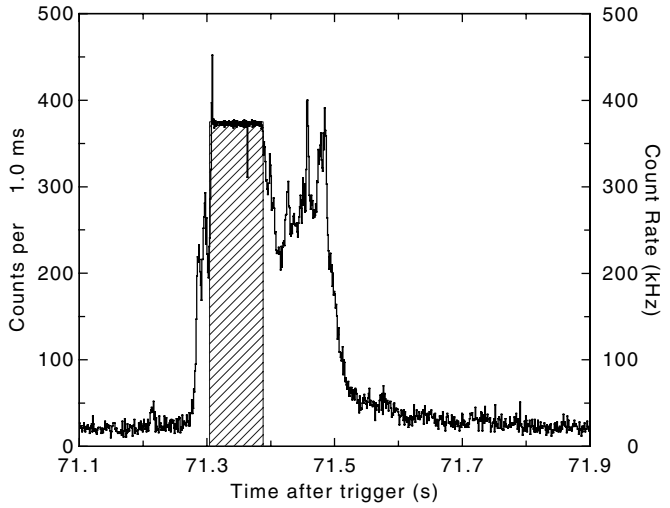


**Figure 1.** One of the 23 saturated SGR J1550−5418 bursts (06:59:34 UT on 2009 January 22). The light curve is the sum of the count rates in all 14 detectors across the entire energy range of GBM. The saturated time interval is indicated by the hatched area.

the peaks. Applying these criteria to our initial list of events, we collected 286 bursts from January 22 to 29, which is the sample we used for our detailed temporal and spectral analysis.

There is a caveat, however, associated with our sample completion. For a significant fraction of the time, we were not able to detect SGR J1550−5418 with GBM: during *Fermi* passages through the South Atlantic Anomaly (SAA) and when the source was occulted by the Earth. Specifically, on January 22, *Fermi* was in the SAA for 3.5 hr and SGR J1550−5418 was occulted by the Earth for almost 8 hr. Since some of these times overlap, the total time that GBM could not detect bursts from SGR J1550−5418 was ∼11 hr. To obtain a complete picture of the source activity, we searched the data of other satellites that were triggered by the source. The only instrument with a continuous SGR J1550−5418 coverage during the entire day of 2009 January 22 was the *INTEGRAL*/SPI-ACS. The SPI-ACS, however, has a higher energy threshold (>80 keV) and provides no energy resolution. As a result it detected fewer bursts (slightly over 200; Mereghetti et al. 2009b), of which only 84 were also detected by the *INTEGRAL*/IBIS/ISGRI instrument, and for which spectral information (>20 keV) was available (Savchenko et al. 2010). Thus, the GBM sample is by far the most complete uniform data set for that entire day's activity from SGR J1550−5418.

For each one of the 286 GBM bursts, we used the TTE data of those NaI detectors that had a source viewing angle (angle between the source direction and the detector normal) of less than 60°. We then checked whether each one of these detectors had an unobstructed view of SGR J1550−5418, i.e., if no parts of the spacecraft or the Large Area Telescope (LAT) on board *Fermi* were obstructing the view. This last check is important because several bursts had such a high peak flux that they caused Autonomous Repoint Requests of *Fermi*, leading to the repointing of the spacecraft to the source. The final orientation in those cases was 5° off from the LAT zenith, resulting in the LAT obstructing the view for some detectors.

Finally, several bursts in our sample were so bright that they saturated the High Speed Science Data Bus of GBM. This effect occurs when the total TTE count rate of all detectors exceeds a limit of 375,000 counts $s^{-1}$. Out of the 286 bursts only 23 were affected; an example of a saturated burst is shown in Figure 1 (hatched area). We did not use the saturated bursts in our temporal analyses (Section 3), since the durations, emission times, and peak times of these bursts are severely affected. We performed a spectral analysis using the non-saturated parts of these bursts, and used their fluences only in the compilation of the cumulative energy fluence emitted during the active period of SGR J1550−5418 (Section 4). None of the 23 saturated bursts were used in any of the other parts of the spectral analysis and discussion sections in this paper.

**Table 1**
Temporal Analysis of 263 SGR J1550−5418 Bursts

| Parameter | Fit Mean[a] | $\sigma$[b] | Mean |
|---|---|---|---|
| $T_{90}$ (ms) | 174 ± 10 | 0.41 ± 0.02 | 258 |
| $T_{50}$ (ms) | 55 ± 4 | 0.46 ± 0.03 | 104 |
| $\tau_{90}$ (ms) | 97 ± 3 | 0.33 ± 0.01 | 127 |
| $\tau_{50}$ (ms) | 29 ± 2 | 0.34 ± 0.02 | 39 |
| $\delta_{90}$ | 0.60 ± 0.03 | 0.24 ± 0.04 | 0.58 |
| $\delta_{50}$ | 0.56 ± 0.03 | 0.25 ± 0.03 | 0.54 |

**Notes.**
[a] log-normal fit for $T_{90,50}$ and $\tau_{90,50}$, normal fit for $\delta_{90,50}$.
[b] In the log-frame except for $\delta_{90,50}$.

## 3. TEMPORAL ANALYSIS

To characterize the temporal properties of all the bursts in our sample, we determined their durations, emission times, duty cycles, and rise times. We calculate these quantities using TTE data binned at 2 ms resolution in the 8–100 keV energy range. We apply a two-step background subtraction method to the total number of counts during and around the burst time interval; details on the particular method used here are given in Göğüş et al. (2001) and Lin et al. (2011).

The $T_{90}$ ($T_{50}$) duration is the time during which 90% (50%) of the total burst counts are accumulated (Kouveliotou et al. 1993). Another parameter to quantify burst durations is the emission time $\tau_{90}$ ($\tau_{50}$) (Mitrofanov et al. 1999). In contrast with $T_{90,50}$, the emission time does not necessarily span a time interval of consecutive time bins; it is computed by adding time bins ordered from the highest to the lowest number of counts until 90% or 50% of the burst counts is accumulated. We then calculated for each burst the duty cycle $\delta_{90}$ ($\delta_{50}$), which is the ratio of $\tau_{90}$ ($\tau_{50}$) over $T_{90}$ ($T_{50}$); this quantity gives an indication of how sharply peaked a given burst light curve is (Mitrofanov et al. 1999). The final temporal parameter we determined is the burst rise time $T_{\rm rise}$ (the time for a burst to reach its peak count rate); in multiple-peaked events, we used the highest count rate bin as the peak.

The results of our temporal analysis are shown in Figure 2 and Table 1. Figure 2 shows the distributions of $T_{90,50}$ (first column panels), $\tau_{90,50}$ (second column panels) and $\delta_{90,50}$ (third column panels), and $T_{\rm rise}/T_{90}$ for single-peaked and multiple-peaked events (fourth column panels). We fit the distributions of the durations and emission times with log-normal functions, and the duty cycle distributions with normal functions. The means and standard deviations of these functions are given in Table 1, together with their normal mean values.

Next, we used the $T_{90,50}$ values and their uncertainties to construct their probability density functions (PDFs) as described in Lin et al. (2011). For each individual PDF, we adopted a two-sided normal distribution with the widths given by the measured

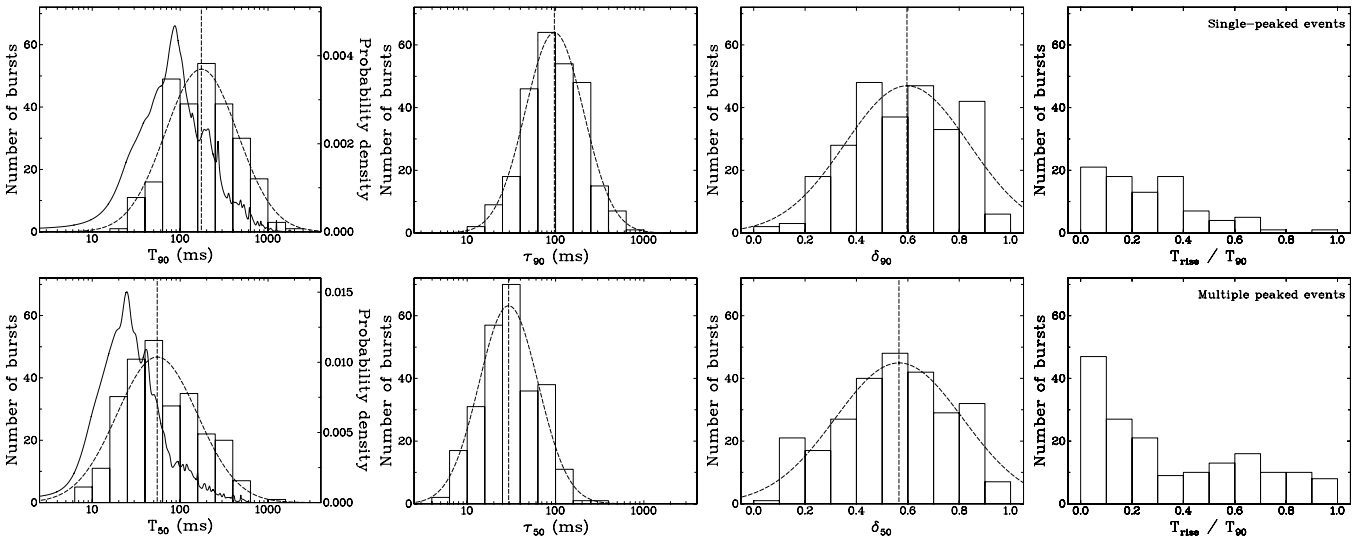


**Figure 2.** Distributions of the durations $T_{90,50}$ (first column panels), emission times $\tau_{90,50}$ (second column panels), duty cycles $\delta_{90,50}$ (third column panels), and $T_{\rm rise}/T_{90}$ (fourth column panels) for single-peaked (top) and multiple-peaked (bottom) events. The dashed lines show the best-fit log-normal ($T_{90,50}$ and $\tau_{90,50}$) and normal ($\delta_{90,50}$) functions, with the vertical dashed lines indicating the fitted mean values. For $T_{90,50}$, the probability density functions are shown as solid lines.

(asymmetric) uncertainties (Starling et al. 2008). Figure 2 shows the average of all the individual PDFs for $T_{90,50}$. Note that the PDFs peak at smaller values than the duration histograms, namely, at ∼85 ms and ∼25 ms for $T_{90}$ and $T_{50}$, respectively. This is due to the fact that the shorter (and weaker) events have relatively larger asymmetries in their uncertainties.

The histograms shown in Figure 2 for the various temporal parameters are typical of magnetar bursts, although there may be variations between different sources (e.g., Göğüş et al. 2001; Gavriil et al. 2004; Lin et al. 2011). The mean $T_{90}$ values in the GBM energy band typically range between 0.1 and 0.2 s, while $\tau_{90}$ ranges are 0.05–0.1 s, resulting in duty cycles of 0.4–0.6 (see also Lin et al. 2011). Our mean $T_{90}$ values for SGR J1550−5418 are larger than those found for *INTEGRAL* (68 ms; Savchenko et al. 2010), but smaller than the *Swift* bursts (305 ms; Scholz & Kaspi 2011). This is due to the different sensitivities and energy ranges of the instruments (see also Scholz & Kaspi 2011). Regarding the rise times, we confirm what has been established for other magnetar bursts (e.g., Göğüş et al. 2001; Scholz & Kaspi 2011): the asymmetric $T_{\rm rise}/T_{90}$ distributions for single-peaked events indicate that magnetar bursts have shorter rise than decay times, and the bimodal distribution of multiple-peaked events shows that for most bursts the first peak is the brightest. In Section 5, we elaborate further on the correlation of the temporal and spectral properties of SGR J1550−5418, and compare these to similar correlations in other magnetar sources.

## 4. SPECTRAL ANALYSIS

We performed time-integrated spectral analysis of all 286 bursts in our sample using the spectral analysis software package *RMFIT* (*3.3rc8*), which was developed specifically for GBM data analysis. For every burst, we selected intervals of background without bursts present before and after a burst, and fit them with a polynomial of the third or fourth order. For the spectral fits we generated detector response matrices using *GBMRSP v1.81*. To obtain the best-fit parameters for any given spectral model, we minimized the Castor *C*-statistic (*C*-statistic hereafter). This method is used to fit data with a low number of counts and is a modification[20] of the Cash statistic so that it asymptotically distributes as $\chi^2$.

We fit various spectral models to the TTE data of each burst: a power law (PL), a blackbody (BB) function, optically thin thermal bremsstrahlung (OTTB), a PL with an exponential cutoff (Comptonized model), a combination of a PL and a BB function (PL+BB), and two BB functions (BB+BB). Figure 3 shows spectra of one of our brightest bursts (using only the unsaturated parts), whose light curve is shown in Figure 1. We have used in this spectral analysis counts from four NaI detectors following the detector selection criteria given in Section 2. The $\nu F_\nu$ spectra in Figure 3 show fits with the six different spectral models mentioned above and their fit residuals. The fit residual trends shown here are very similar for all bursts in our sample, with the brightest bursts presenting the strongest trends. From Figure 3, an obvious conclusion would be that OTTB, Comptonized, and BB+BB fits provide a better description of the data than PL, BB, or PL+BB. In Section 4.1, we attempt to quantify this statement. We note that the apparent feature between 30 and 40 keV in the fit residuals is a result of the NaI K-edge, which has not been modeled perfectly in the GBM calibration (Bissaldi et al. 2009). We have performed fits with and without the K-edge energy channels, and found that their inclusion does not change any of the fit parameters significantly, therefore we included these channels in all fits for better statistics.

### 4.1. Simulations

We have performed extensive simulations with *RMFIT* (3.4rc3) to evaluate the effect of statistical fluctuations on identifying the best model to describe SGR burst spectra. For this purpose, we selected six bright bursts (two from SGR J1550−5418 and three from SGR J0501 + 4516; see also Lin et al. 2011), and compared pairs of various models, generating 30,000 synthetic spectra for each burst and each relevant detector. Each synthetic spectrum was based on the sum of the predicted source counts and the measured background counts in each energy channel. The former counts were computed from the analytical function

[20] http://fermi.gsfc.nasa.gov/ssc/data/analysis/user

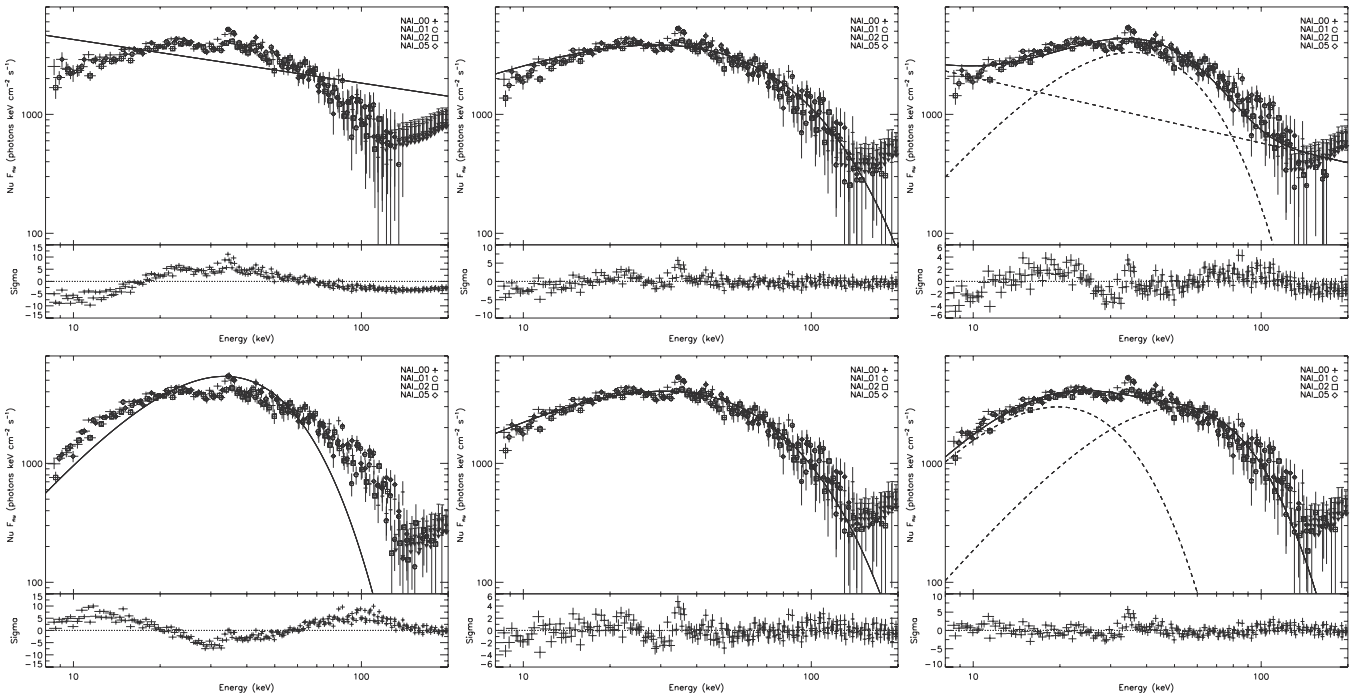


**Figure 3.** Time-integrated $\nu F_\nu$ spectra of one of the brightest SGR J1550−5418 bursts (06:59:34 UT on 2009 January 22), shown in Figure 1, for various spectral models: power law (top left), single black body (bottom left), OTTB (top center), Comptonized (bottom center), power law plus black body (top right), and two black body functions (bottom right). The bottom panel of each spectrum shows the fit residuals. The feature between 30 and 40 keV in the fit residuals is a result of the imperfect modeling of the NaI K-edge.

with the largest *C*-statistic used to fit the real data (null hypothesis) folded with the instrumental response function of the relevant detector (as a check, we also used as null hypothesis the function giving the lowest *C*-statistic and we obtained consistent results). The background counts were estimated for each detector from the real data. Next, we applied Poisson fluctuations to the summed counts to obtain the final synthetic spectrum.

During the fit process, we generated a synthetic background spectrum by adding Poisson fluctuations to the real background estimate in each energy channel and subtracting it from the synthetic spectrum. The resulting spectrum was fitted with the two models of each pair. We checked and confirmed that the input spectral parameters were well recovered in the fits of the synthetic spectra by comparing them and their statistical errors to the simulated parameter distributions and their uncertainties. Finally, to test whether this recovery was intensity dependent, we also simulated two weak events and arrived at the same conclusions.

We then proceeded to compare the fits between different model pairs. To this end, we computed the *C*-statistic difference between one input model and each other spectral model for all 30,000 synthetic spectra per burst, and compared the resulting distribution to the difference obtained using the same models with the real burst data.

First, we compared PL and BB with all other spectral models, because the former systematically gave the largest fit residual patterns for the majority of the events in our sample. For all simulated events, we found that statistical fluctuations in the signal and background cannot explain that OTTB or any of the more complex models fit the data better than PL or BB, including the weakest one with a fluence of $6.7 \times 10^{-8}$ erg cm$^{-2}$. Using the same procedure, we then compared all the other models, namely, OTTB, Comptonized, PL+BB, and BB+BB. Our simulations showed that the statistical fluctuations in the data could account for the difference in *C*-statistic values between these models, preventing us from drawing conclusions on the best spectral shape. We cross-checked and confirmed the results of our simulations using XSPEC (v12.6; Arnaud 1996). We conclude, therefore, that we cannot unambiguously determine whether OTTB, Comptonized, PL+BB, or BB+BB is the best spectral fit model for our burst sample.

The same method has been used to distinguish between spectral models for gamma-ray bursts detected with GBM (see, e.g., Guiriec et al. 2011), albeit resulting in identification of the best-fit spectral model. The discrepancy with the SGR simulation results here could be explained by the fact that even the brightest SGR bursts have a lower total number of source counts mostly distributed over a much narrower energy range (10–50 keV).

### 4.2. Spectral Model Selection

Although our simulation results were inconclusive regarding the preferred spectral model, we attempt here to narrow down the number of models that give a good description of the SGR burst spectra. We did this down-selection based on the following arguments. When fitting the spectra of individual bursts, we obtained systematically large fit residual patterns with the PL, BB, and PL+BB functions for a large fraction of the events in our sample; all other model residuals were randomly distributed. For the PL and BB models, we showed in Section 4.1 that they give a worse description of the data than all other models for bursts with fluences above $6.7 \times 10^{-8}$ erg cm$^{-2}$. In addition, the PL and BB models predominantly had the largest *C*-statistic values for all bursts compared to all other models, resulting in very large *C*-statistic differences, typically tens to hundreds and for some events even a few thousand. This difference increased with fluence, indicating that the brightest events are worst fit with a PL or BB. Such a dependence on brightness was not

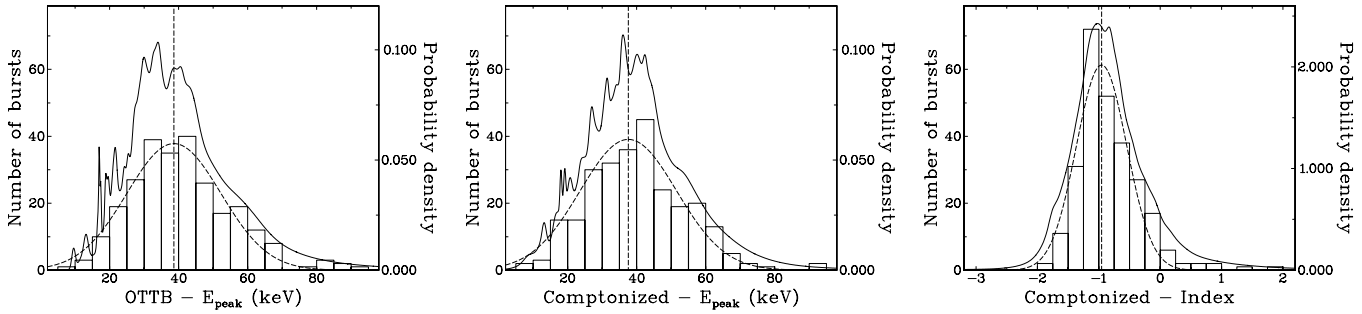


**Figure 4.** Distributions of the OTTB $E_{\rm peak}$ (left), Comptonized $E_{\rm peak}$ (middle), and of the Comptonized power-law index (right). The dashed lines show the best-fit normal functions, with the vertical dashed lines indicating the fitted mean values. The probability density functions are shown as solid lines.

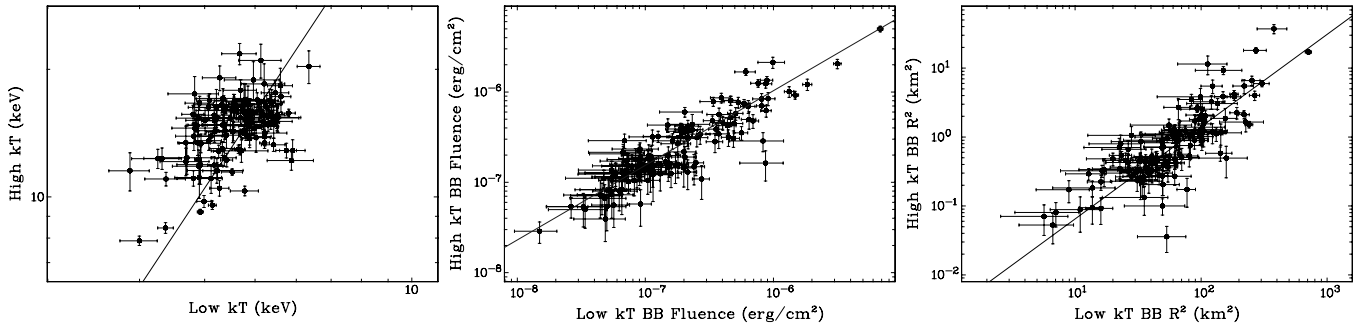


**Figure 5.** Correlations between the cool and hot blackbody parameters: temperatures (left panel), fluences (middle panel), and emission areas (right panel).

seen when comparing *C*-statistic differences between all other models. The combination of all these arguments led us to discard PL and BB models from further analysis for bursts at all fluences. Our PL+BB fits gave a *C*-statistic value better than OTTB for only one-third of the bursts in our sample, while PL+BB has two more free parameters than OTTB. Moreover, the PL+BB model systematically gave residual patterns not seen in the BB+BB, Comptonized, and OTTB fits. We, therefore, excluded the former model from further consideration.

It is not possible to exclude any of the three remaining models, namely, OTTB, Comptonized, and BB+BB. We cannot choose between OTTB and Comptonized because the PL index we retrieve in the Comptonized fits is often very close to $-1$ (in photon space) and OTTB is basically a special case of Comptonized with an index of $-1$. This is illustrated in the rightmost panel of Figure 4, which shows the distribution of the Comptonized PL indices for all events, together with a normal fit to the distribution with a mean value of $-0.95$ and a width of 0.41. Finally, BB+BB is very similar to the Comptonized function over this relatively small energy range (e.g., see the bottom middle and bottom right panels of Figure 3). When comparing the *C*-statistic for individual bursts, the difference between these two models lies almost always between $-25$ and 25, with the majority between $-10$ and 10, making the choice of the best fit very difficult. We, therefore, describe below our results of the spectral fits on all 263 events using the OTTB, Comptonized, and BB+BB models.

### 4.3. OTTB and Comptonized Model

The first two panels in Figure 4 show the $E_{\rm peak}$ distributions for the OTTB (left panel) and the Comptonized (middle panel) models. We note that these are very similar with mean $E_{\rm peak}$ values of 39 keV and widths of 13 keV in both cases. The OTTB function has been applied successfully to SGR bursts detected with instruments that have a spectral coverage similar to or smaller than GBM (e.g., Göğüş et al. 1999, 2000, 2001). Several studies, however, have shown that if the spectral range is extended down to several keV, OTTB overestimates the flux at lower energies (e.g., Fenimore et al. 1994; Feroci et al. 2004). Figure 3 indicates a small trend for overestimation below 10 keV, and a similar hint is seen in several other bright bursts in our sample. Figure 3 also shows that a Comptonized function with an index of $\sim -0.7$ corrects for this possible trend. For the brightest bursts, pulse pile-up could affect the burst hardness, which would be reflected in the index value. We have performed simulations to study this effect, and for the count rates observed in our brightest bursts, the Comptonized index becomes flatter by at most 0.1, while the $E_{\rm peak}$ value does not change significantly. Given that the GBM calibration (Bissaldi et al. 2009) was done for energies starting at $\sim$14 keV and then extrapolated to lower energies, at this point we cannot determine the significance of a Comptonized index deviation of 0.3 from $-1$. We thus compare in Section 5 the spectral parameters derived with both models to other SGR sources.

### 4.4. Two Blackbody Models

As an alternative to OTTB or Comptonized, several studies have shown that SGR bursts can be fit well with two BB functions (e.g., Feroci et al. 2004; Olive et al. 2004; Nakagawa et al. 2007; Israel et al. 2008; Esposito et al. 2008; Lin et al. 2011). We have fit 263 of our bursts in our sample (excluding the 23 saturated events) with BB+BB. Several of these, however, were faint and their parameters could not be well constrained. Therefore, in the following we have limited our sample to those bursts for which the temperatures and fluences of both BBs have values that are at least two times larger than their uncertainties, resulting in a final sample size of 123 bursts. The left panel of Figure 5 shows the correlation of temperatures for the low- and high-temperature BB; the average values (and widths) of the

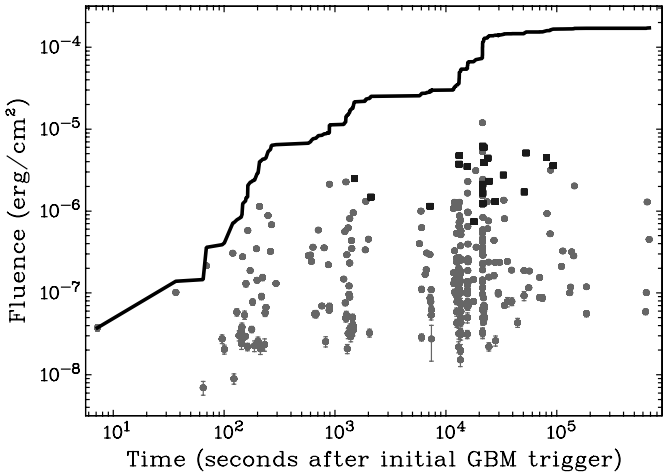


**Figure 6.** Cumulative distribution (solid line) of the energy fluence for all 286 bursts in our sample. The gray data points are individual burst fluences and the black squares indicate bursts that are partially affected by saturation.

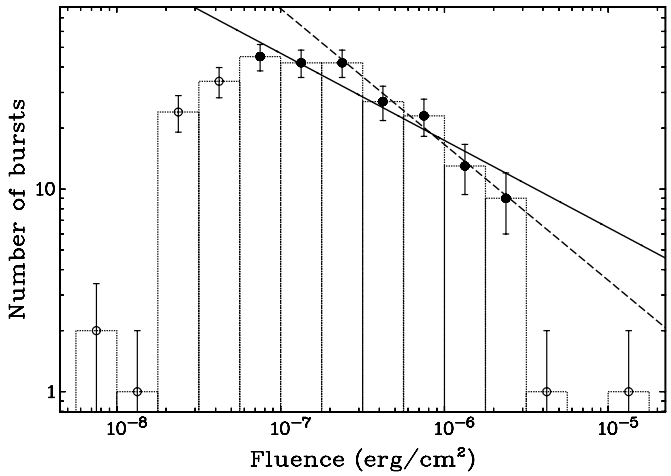


**Figure 7.** Differential distribution of the energy fluence of SGR J1550−5418 bursts on a logarithmic scale. The solid line shows the best power-law fit to the solid circles, ranging from $10^{-7.25}$ to $10^{-5.50}$ erg cm$^{-2}$, with an index of $-0.4 \pm 0.1$. The dashed line shows the fit of fluences ranging from $10^{-6.75}$ to $10^{-5.50}$ erg cm$^{-2}$, with a power-law index of $-0.7 \pm 0.2$. The histogram error bars indicate $\sqrt{N}$ with $N$ the number of bursts per fluence histogram bin. Note here that the lower fluence turnover may be reflecting either instrumental sensitivity or an intrinsic source property, or a combination of both. Therefore, we give a range for the power-law slopes.

log-normal distributions for the cool and hot BB are 4.6 (0.7) and 14.8 (2.1) keV, respectively.

Figure 5 (middle and right panels) also shows the correlations between the fluences and emission areas of both BBs. We estimated the significance of these correlations with a Spearman rank order correlation test. In the following, we designate a correlation to be significant if the chance probability, $P < 5.7 \times 10^{-7}$, corresponding to $5\sigma$, when the correlation coefficient follows a normal distribution; a correlation is marginally significant if $5.7 \times 10^{-7} < P < 2.7 \times 10^{-3}$ ($3\sigma$). While the temperature correlation is almost significant at the $5\sigma$ level, with $P = 7 \times 10^{-7}$, the fluences and emission areas are very strongly correlated. When fitted by a PL, the slopes of the correlations are $1.86 \pm 0.09$, $0.83 \pm 0.02$, and $1.34 \pm 0.04$, for all three panels, respectively. We further discuss these correlations in Section 5.

## 5. DISCUSSION

We discuss here the energetics of the SGR J1550−5418 bursts using our spectral fitting results. We describe the correlations between the spectral and temporal parameters, and compare our results to the ones of other sources in the literature. Finally, we expand on the interpretation of our BB+BB model results.

### 5.1. Burst Energetics

We have determined the energy fluence for all the bursts in our sample in the 8–200 keV energy range. The fluence values obtained with our three preferred models (OTTB, Comptonized, and BB+BB) are very similar. In the following, we present the fluences for the Comptonized fits only, because the model has one less parameter than BB+BB, and there are several events with PL indices deviating from −1 (corresponding to OTTB). Figure 6 shows the cumulative energy fluence during the source burst active period as well as the individual burst fluences. To obtain the best estimate of the total fluence released during that period in bursts, we have used data from all 286 bursts, including saturated events (black squares) whose values are merely lower limits. The fluence range spanned in our sample is rather large, $\sim 10^{-8}$ to $\sim 10^{-5}$ erg cm$^{-2}$, which is comparable to the range of SGR J0501+4516 bursts observed with GBM (Lin et al. 2011) and larger than previous studies of other magnetars (Göğüş et al. 2001; Gavriil et al. 2004). This fluence range corresponds to an energy range in bursts of $\sim 3 \times 10^{37}\, d_5^2$ to $\sim 3 \times 10^{40}\, d_5^2$ erg, which is comparable to the values found for other SGRs, but orders of magnitude higher than AXP 1E 2259+586 (Gavriil et al. 2004).

The total energy fluence in bursts recorded with GBM alone is $1.7 \times 10^{-4}$ erg cm$^{-2}$, which is in fact a lower limit given that there were saturated bursts, as well as bursts we excluded from our analysis since no TTE data were available, or bursts that GBM did not detect because of the SAA or Earth occultation. This results in a lower limit on the energy emitted in bursts of $5 \times 10^{41}\, d_5^2$ erg, which is four orders of magnitude larger than the total energy in bursts from AXP 1E 2259+586 in 2002 June (Gavriil et al. 2004). The SGR J1550−5418 bursts detected with *INTEGRAL*/SPI-ACS on 2009 January 22 had an estimated cumulative fluence of $5.2 \times 10^{-4}$ erg cm$^{-2}$ (25 keV–2 MeV; Mereghetti et al. 2009b), i.e., a cumulative energy of $1.6 \times 10^{42}\, d_5^2$ erg. The total energy released in bursts detected with the *Swift* X-ray Telescope (XRT) was much lower, namely, $1.6 \times 10^{40}\, d_5^2$ erg (1–10 keV; Scholz & Kaspi 2011). Scholz & Kaspi (2011) argue that the energy released in bursts is smaller than the energy released in the persistent emission between 2009 January and September over that same energy range, i.e., $1.5 \times 10^{42}\, d_5^2$ erg. They further claim that this behavior is similar to the one observed in AXP 1E2259+586 and not in agreement with an SGR persistent emission. Although the persistent emission energy release cannot be directly measured by GBM or SPI-ACS, Bernardini et al. (2011) have shown that for that same time period, it can be at most a factor of five higher in the 13–200 keV than in the 1–10 keV range. The energy released in bursts during a week is thus comparable to the energy released in the persistent emission during an eight-month period (Scholz & Kaspi 2011), and we conclude that SGR J1550−5418 exhibits similar energetics behavior as other SGR sources (Woods et al. 2004).

We plot in Figure 7 the differential fluence distribution for the 263 unsaturated bursts. The distribution is fitted, using unbinned maximum likelihood, between $10^{-7.25}$ and $10^{-5.50}$ with a PL of index $-0.4 \pm 0.1$, and between $10^{-6.75}$ and $10^{-5.50}$ with an

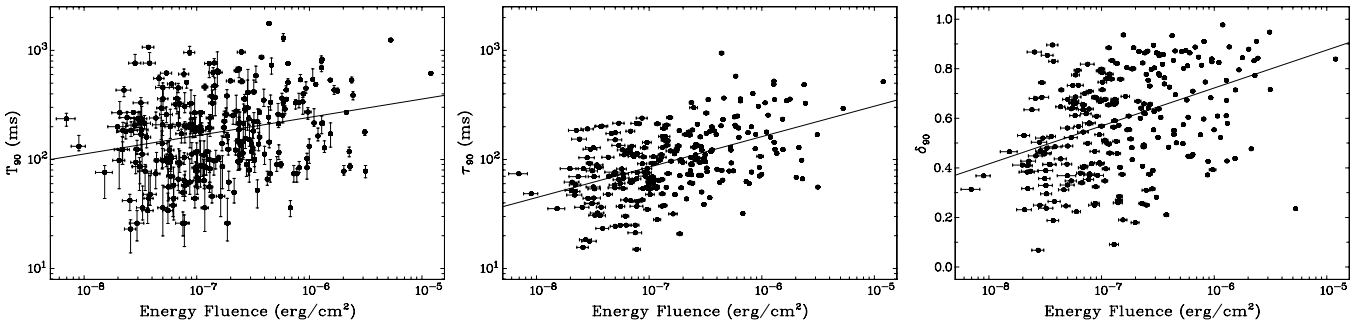


**Figure 8.** Correlation plots of $T_{90}$, $\tau_{90}$, and $\delta_{90}$ vs. energy fluence. The lines indicate power-law fits to the data.

**Table 2**
Spearman Rank Order Correlation Coefficients and Probabilities for Various Spectral and Temporal Parameters

| Parameters | Coefficient | Probability |
|---|---|---|
| $E_{\rm peak}$–Fluence[a] | −0.444 | $3.7 \times 10^{-14}$ |
| $T_{90}$–Fluence[b] | 0.229 | $1.8 \times 10^{-4}$ |
| $T_{50}$–Fluence | 0.121 | $4.9 \times 10^{-2}$ |
| $\tau_{90}$–Fluence[a] | 0.470 | $6.0 \times 10^{-16}$ |
| $\tau_{50}$–Fluence[b] | 0.236 | $1.1 \times 10^{-4}$ |
| $\delta_{90}$–Fluence[a] | 0.391 | $4.6 \times 10^{-11}$ |
| $\delta_{50}$–Fluence[b] | 0.193 | $1.6 \times 10^{-3}$ |
| $T_{90}$–$E_{\rm peak}$ | −0.071 | 0.25 |
| $T_{50}$–$E_{\rm peak}$ | 0.029 | 0.64 |
| $\tau_{90}$–$E_{\rm peak}$[b] | −0.209 | $6.5 \times 10^{-4}$ |
| $\tau_{50}$–$E_{\rm peak}$ | −0.086 | 0.16 |
| $\delta_{90}$–$E_{\rm peak}$[b] | −0.252 | $3.4 \times 10^{-5}$ |
| $\delta_{50}$–$E_{\rm peak}$[b] | −0.260 | $1.9 \times 10^{-5}$ |

**Notes.**
[a] Significant correlation.
[b] Marginally significant correlation.

index $-0.7 \pm 0.2$. This corresponds to $dN/dF \propto F^{-1.4}$ and $dN/dF \propto F^{-1.7}$, respectively. The turnover in the distribution at the low-fluence end is most likely caused by instrumental sensitivity drop-off; the onset of the turnover is not well determined and it depends on the criteria of the untriggered burst search algorithm. The high-fluence end of the distribution reflects that our sample is not complete with high-fluence bursts. When only taking the fluences above $10^{-6.75}$ erg cm$^{-2}$, the PL index is comparable to the values of $\sim -0.7$ found for some other magnetar sources (Woods & Thompson 2006; Gavriil et al. 2004). The shallower value we obtain by including fluences down to $10^{-7.25}$ erg cm$^{-2}$ is closer to the values for SGR 1806−20 (Göğüş et al. 2000) and SGR J0501+4516 bursts (Lin et al. 2011).

### 5.2. Spectral and Temporal Correlations

Several authors have investigated correlations between the various spectral and temporal parameters of SGR bursts (e.g., Göğüş et al. 2001; Gavriil et al. 2004). Here, we again present analysis using only the results of our Comptonized model fits. Using the Spearman rank order correlation test, we have searched for possible correlations between $E_{\rm peak}$, index, fluence, and the temporal parameters $T_{90,50}$, $\tau_{90,50}$, and $\delta_{90,50}$. There are no significant correlations between the index and any other parameter; for all the other correlations the Spearman rank correlation coefficients and chance probabilities are listed in Table 2. From Table 2, it follows that the $T_{90}$ duration is marginally correlated with fluence. The emission time $\tau_{90}$ is strongly correlated with fluence and the same is true for $\delta_{90}$, while the correlations for $\tau_{50}$ and $\delta_{50}$ are only marginal. Figure 8 shows the correlations of $T_{90}$, $\tau_{90}$, and $\delta_{90}$ versus fluence; it is apparent that there is a stronger correlation for $\tau_{90}$ than for $T_{90}$ or $\delta_{90}$. When fitting a PL to these correlations, we obtain indices of $0.17 \pm 0.04$ for $T_{90}$, $0.28 \pm 0.03$ for $\tau_{90}$, and $0.11 \pm 0.02$ for $\delta_{90}$.

There is no significant correlation between $E_{\rm peak}$ and the duration or emission time, and there is a marginal anti-correlation between $E_{\rm peak}$ and the duty cycle. $E_{\rm peak}$, however, is strongly anti-correlated with fluence, which is also clear from the top panel of Figure 9. The bottom panel of that figure shows a significant anti-correlation between $E_{\rm peak}$ and the average burst flux, with a Spearman rank correlation coefficient of −0.344 and a chance probability of $9.4 \times 10^{-9}$. Since the Comptonized index does not depend significantly on the fluence of the bursts, $E_{\rm peak}$ is a good indicator of the hardness of bursts. Therefore, we can conclude that there is an anti-correlation between hardness and fluence, and between hardness and average flux, for the SGR J1550−5418 bursts. When we fit $E_{\rm peak}$ versus fluence with a PL, we obtain an index of −0.093, while an $E_{\rm peak}$ versus average flux fit gives an index of −0.042 (dashed lines in both panels of Figure 9).

The bottom panel of Figure 9 indicates that there may be a more complicated trend for $E_{\rm peak}$ versus average flux than a single PL. Similar to what has been found for the time-resolved spectroscopy of SGR J0501+4516 bursts detected with GBM (Lin et al. 2011), we find an anti-correlation at low flux values, but a positive correlation at high flux values. We fit this trend with a broken PL with indices of −0.22 and 0.07, with the turning point occurring at an $E_{\rm peak}$ of 30 keV and at an average flux of $4 \times 10^{-6}$ erg s$^{-1}$ cm$^{-2}$. An $F$-test gives an improvement of $4\sigma$ (chance probability of $8 \times 10^{-5}$) for a broken PL compared to a single one. We note that a Spearman rank order correlation test for the fluxes below $4 \times 10^{-6}$ erg s$^{-1}$ cm$^{-2}$ gives a coefficient of −0.256 and a chance probability of $7.2 \times 10^{-5}$, i.e., $\sim 4\sigma$ significance, while for fluxes above $4 \times 10^{-6}$ erg s$^{-1}$ cm$^{-2}$ there is not a significant positive correlation with a coefficient of 0.085 and probability of 0.64.

The minimum average flux defined by the broken PL fit is a factor of two lower than the corresponding flux found for SGR J0501+4516 by Lin et al. (2011). Given that SGR J0501+4516 has an estimated distance of ∼2 kpc, the minimum of an $E_{\rm peak}$–luminosity correlation is three times larger for SGR J1550−5418 than for SGR J0501+4516. However, given the uncertainties in the source distances and in the determination of the minima in the correlations, these differences are not significant. Furthermore, these correlations were obtained from time-resolved spectroscopy in the case of SGR J0501+4516, while we present here only time-integrated results for SGR J1550−5418;

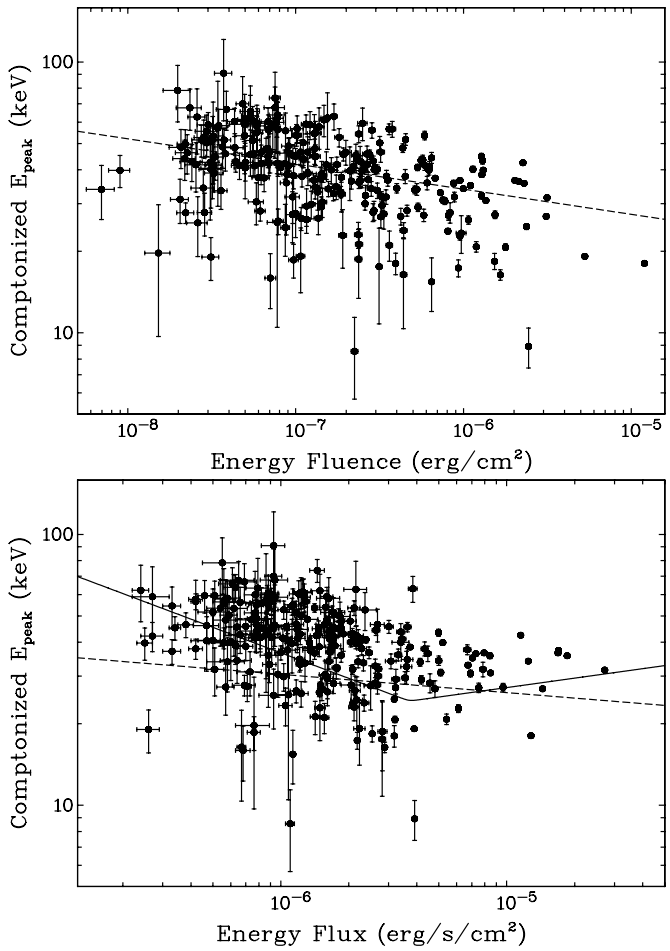


**Figure 9.** Correlation plot between Comptonized $E_{peak}$ and energy fluence (top panel) and average energy flux (bottom panel). The dashed lines indicate a power-law fit, while the solid line in the bottom panel indicates the result of a broken power-law fit.

time-resolved analysis of the brightest SGR J1550−5418 bursts is part of a future study. Note that in contrast with Lin et al. (2011), in the $E_{peak}$–fluence correlation a broken PL does not give an improvement over a single PL.

The correlation or anti-correlation between hardness and brightness of magnetar bursts has been discussed by several authors (e.g., Göğüş et al. 2001; Gavriil et al. 2004; Götz et al. 2004). The spectral range and temporal capabilities of GBM allow us to characterize the burst spectral hardness with $E_{peak}$, as was also done in Lin et al. (2011). This hardness indicator is much better defined than hardness ratios or indices of single PL spectral fits. Further, our bursts span a larger fluence and flux range than any other studies with comparable sample size. Using large samples of bursts from SGRs 1806−20 and 1900+14 observed with *RXTE*, Göğüş et al. (2001) have shown that there is an anti-correlation between hardness and brightness based on hardness ratios between 10–60 and 2–10 keV. The same anti-correlation was found by Götz et al. (2004) who performed a similar analysis on *INTEGRAL*/IBIS data for SGR 1806−20 using hardness ratios between 40–100 and 15–40 keV. Contrary to the above results, Gavriil et al. (2004) showed a positive correlation for bursts of AXP 1E2259+586 detected with *RXTE*, also using hardness ratios, and concluded that this behavior distinguishes AXPs from SGRs.

For SGR J1550−5418, Savchenko et al. (2010) found a positive correlation between hardness and brightness based on *INTEGRAL*/SPI-ACS hardness ratios between 60–200 and 20–60 keV. However, Scholz & Kaspi (2011) do not find a hardness–fluence correlation in the *Swift*/XRT bursts on 2009 January 22. They then fit a single PL to the burst spectra, and find a significant anti-correlation between the index and flux, indicating a positive correlation between hardness and brightness. Based on this correlation, Scholz & Kaspi (2011) have argued for an AXP nature of SGR J1550−5418. We discuss below why the results from Savchenko et al. (2010) and Scholz & Kaspi (2011) are in apparent disagreement with our $E_{peak}$–fluence and $E_{peak}$–flux anti-correlations. The energy ranges used by Savchenko et al. (2010) and Scholz & Kaspi (2011) bracket the energy ranges used by Göğüş et al. (2001) and Gavriil et al. (2004). It is not trivial to compare hardness ratios over different energy ranges, given that the SGR burst peak emission is in the low energy band for Savchenko et al. (2010) and in the high energy band for Göğüş et al. (2001) and Gavriil et al. (2004). More importantly, we have shown here that a single PL does not provide a good description for the SGR J1550−5418 burst spectra, which makes the method of Scholz & Kaspi (2011) less effective than using $E_{peak}$ as a hardness indicator. Taking all these arguments into account, we conclude that the GBM hardness–fluence anti-correlation of SGR J1550−5418 strongly indicates that the source is very similar to other SGR sources.

### 5.3. Comparison with Other SGR Sources

#### 5.3.1. OTTB and Comptonized Model

Since OTTB or Comptonized models have very often been used as the best models for SGR bursts, we now compare our spectral fit parameters with those from studies of other SGR sources. Our $E_{peak}$ distributions (Figure 4) are very typical for SGR bursts, but there seems to be a difference across SGR sources regarding the PL indices of the Comptonized function. The average PL index for SGR J1550−5418 bursts (−0.95) is significantly different than the one found by Lin et al. (2011) for a sample of 29 bursts detected by GBM from SGR J0501+4516, namely, −0.32. Although the width of the index distribution is fairly large for SGR J0501+4516, 0.9 compared to 0.41 for SGR J1550−5418, Lin et al. (2011) show that their brightest bursts have well-constrained indices close to 0, significantly deviating from −1. Feroci et al. (2004) have fit 10 short bursts detected by *BeppoSAX* from SGR 1900+14 with a Comptonized function, and they find a mean spectral index of −0.4 with a dispersion of 0.2. Their result is comparable to the SGR J0501+4516 bursts and not consistent with our values for SGR J1550−5418. The spectral index differences between various SGR sources could be due to differences in magnetic field strength, geometry, plasma temperature, or opacity. Lin et al. (2011) discuss in detail some of the effects the extreme magnetic fields of magnetars have on the Comptonized PL index. More detailed studies, both theoretically and observationally, are needed to reach conclusive results.

#### 5.3.2. Two Blackbody Model

The temperatures, fluences, and areas we find for the BB+BB model are similar to those of other SGR sources (e.g., Feroci et al. 2004; Olive et al. 2004; Nakagawa et al. 2007; Israel et al. 2008; Esposito et al. 2008; Lin et al. 2011). We have found

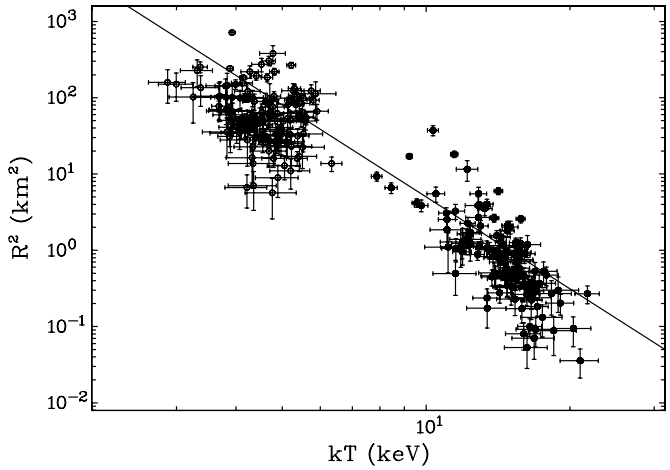


**Figure 10.** Emission area as a function of blackbody temperature for those bursts in our sample that have well-constrained parameters in a BB+BB fit. The solid line indicates $R^2 \propto (kT)^{-4}$ (see the text for a discussion).

a positive correlation between the emission areas of the two BBs (Figure 5), which is more significant than the one found for bursts from SGRs 1806−20 and 1900+14 (Nakagawa et al. 2007). A strong correlation between the two BB luminosities has been found for SGR 1900+14 bursts with *Swift* (Israel et al. 2008) and for SGR J0501+4516 bursts with GBM (Lin et al. 2011). The latter two studies, however, have used time-resolved spectral analyses, while we show here a strong fluence correlation between the two BBs for time-integrated spectra.

Figure 10 displays the emission area as a function of temperature for both BBs. The temperature of the cool BB does not show any correlation with the fluence or the emission area of that BB. The hot BB does have a marginal anti-correlation between temperature and fluence, with a chance probability of $1 \times 10^{-3}$ in a Spearman rank correlation test, and a very strong anti-correlation between the temperature and the emission area (Figure 10) with a chance probability of $3 \times 10^{-24}$. For illustrative purposes, we have drawn a solid line in Figure 10 indicating $R^2 \propto (kT)^{-4}$, which corresponds to a constant burst luminosity or fluence. The line seems to represent best the low-temperature part of the hot BB data, while there is a clear steepening at the higher temperatures. Indeed, a PL fit of the hot BB data gives a slope of $\sim -7$, similar to what has been shown for SGR J0501+4516 by Lin et al. (2011). Similar studies have been performed for SGRs 1900+14 (Israel et al. 2008) and 1627−41 (Esposito et al. 2008) using time-resolved spectroscopy; our results confirm the trends described in these studies. A detailed time-resolved spectroscopy of SGR J1550−5418 bursts is underway.

Finally, we note that the smallest emission areas of the hot BB (few hundredths of km$^2$) are comparable to the emission area of the BB component found during enhanced persistent emission from SGR J1550−5418 in the GBM data after the bursting onset on 2009 January 22 (Kaneko et al. 2010), possibly indicating a common origin of the two phenomena. For the outburst data studied here, the compact hot BB component can be as small as $R \sim 0.2$–$0.3$ km in size, corresponding to a diameter of the order of the thickness of the outer crust, yet the bulk of the $R$-values for the hot BB component correspond to a diameter of $\sim$1 km—comparable to the total thickness of the solid crust. For energy injection at or just below the surface, if these scales signify the size of the region in the crust that is fractured by the magnetic stresses, as is likely, then injection scales considerably smaller than the crust height have greater difficulty in disrupting it and initiating a flare, particularly if the anchored magnetic flux tube is non-radial at its footpoint. To leading order, the field energy that threads the injection region scales as $R^2$, while the length of the required fracture and the corresponding energy required to produce it scale as $R$. Hence, crustal disruption by field twists or shear is expected to be less effective for smaller $R$, a contention that appears to be borne out in the data: the majority of bursts possess $R$ values for the hot component on the scale of the thickness of the crust. Moreover, flares with a larger $R$ for the hot BB component tend to have a larger total energy output, i.e., luminosity or fluence.

### 5.4. Interpretation of Two Blackbody Model Results

The BB+BB model results point toward a photospheric interpretation, and perhaps one with dynamic evolution, from one magnetospheric locale to another. The fitted temperatures exceed those found ($\sim$0.5 keV) in the classic X-ray band (0.5–10 keV) in quiescent magnetar emission (e.g., see Perna et al. 2001), indicating a magnetospheric origin for such photospheres, as opposed to generation of emission purely on the neutron star surface. While it is possible that the site of outburst activation could be near the magnetic poles, the $T_{90}$ durations of SGR J1550−5418 far exceed the neutron star light crossing time. Hence, even the intense magnetic fields of magnetars cannot restrict the emission region of powerful outbursts to small volumes. Accordingly, one expects spatial transport of the burst luminosity during each flare, even if tied to closed field lines. This is essentially the picture that Duncan & Thompson (1992) originally envisaged for SGRs. Polar origins would permit rapid plasma expansion along open field lines to very high altitudes, so that plasma containment is limited. Near the equator, trapping of the gas is optimal, enabling longer durations of emission, so that quasi-equatorial locales for energy injection might be favored. The trapping times depend intimately upon the complicated interplay of polarization-dependent Compton scattering, and associated lepton diffusion and energy exchange within the photon–electron gas.

The core property evinced in Figure 10 is that the burst luminosity $\propto (kT)^4\, R^2$ of the collection of bursts (and approximately also for individual bursts) is similar for the low- and high-temperature components. This is a total energy equipartition feature: if the surface area of a putative magnetospheric emission volume scales approximately as $R^2$, then the energy in each BB component is approximately equal. An $R^2$ scaling most likely applies to the hotter BB component as it evolves in a coronal structure, with photon and particle propagation away from an injection zone. It could be pertinent for burst activation locales near the magnetic poles, but also if the injection site is somewhat remote from the surface, for example, in the magnetospheric twist scenario of Thompson & Beloborodov (2005) and Beloborodov & Thompson (2007), which was primarily envisaged for the lower luminosity, quiescent magnetar emission. However, it is possible that other volume scalings are operating, particularly due to the anisotropizing influence of the non-uniform magnetic field. For example, volumetric constriction of hot plasma near field line footpoints might modify this correlation modestly. Determining the effective volume scaling requires detailed time-dependent modeling of particle and radiative transfer in a magnetospheric environment. This motivates future theoretical work on magnetar "fireballs." Yet, for the present, a baseline conclusion is that it is clear that the strong correlation between the energies in the two components

suggests that they share the same physical origin if BB+BB is indeed the correct model for these bursts.

It is natural to expect that the high-temperature component would be more closely connected to a smaller injection region, where energy is dissipated from crustal stress fractures (Duncan & Thompson 1992; Thompson & Duncan 1995) or some other origin. Proximity of the injection site to the surface is favored in such a scenario, and the resultant fireball of electrons and photons should subsequently expand and cool at higher altitudes in the closed magnetospheric zone, thereby generating the lower temperature component. The injection temperature is controlled by the total energy dissipated by hot electrons present in the inner magnetosphere. The magnetic Thomson optical depth should be high, so that Comptonization will drive thermalization, and the fireball evolution and duration will be influenced by the anisotropic, magnetic Eddington luminosity. Equilibration between photons and electrons will be non-uniform over the coronal volume, so that there should be a modest temperature gradient throughout; the emergent continuum will be a superposition of distorted BBs. In particular, the strong polarization dependence of the anisotropic Compton process naturally establishes two different physical scales for the optically thick environment (Ulmer 1994; Miller 1995), with the so-called E-mode photosphere being smaller than the O-mode photosphere. Perhaps these physically distinct regions assume somewhat different temperatures on average, though a more quantitative development of this picture is beyond the scope of this paper. Whatever the site of the injection, one anticipates that there will be distinctive evolutionary signatures in the dynamic fireball as it either expands to higher altitudes, or contracts when constricted near magnetic footpoints, resulting in a certain temporal evolution for the temperatures. Evolutionary aspects of the spectroscopy of SGR J1550−5418 bursts will be explored in a future paper.

## 6. CONCLUSIONS

We have presented the results of a time-integrated spectral and temporal study of bursts from SGR J1550−5418 during an extremely active bursting period, making optimal use of the spectral and temporal capabilities of GBM. The durations, emission times, and duty cycles are typical of SGR bursts, with burst rise times shorter than their decays. Our spectral analysis shows that the spectra of SGR J1550−5418 bursts are equally well described by OTTB, Comptonized, and BB+BB. The $E_{\rm peak}$ distributions of OTTB and Comptonized have mean values of ∼39 keV, while the Comptonized PL index average is close to −1, i.e., we recover the OTTB index in our Comptonized fits. Whether this PL extends down to lower energies can only be determined by combined fits with other instruments, for instance, *Swift*/XRT (Lin et al. 2012, in preparation).

We have investigated the presence of correlations between the various spectral and temporal parameters, and find significant correlations between the emission time and the fluence, and between the duty cycle and the fluence, and a marginal correlation between the duration and the fluence. We have also shown that there is a significant anti-correlation between $E_{\rm peak}$ and fluence, and between $E_{\rm peak}$ and average flux. We find an anti-correlation at low flux levels but a weak correlation with $E_{\rm peak}$ at high fluxes, with a possible minimum at 4 erg s$^{-1}$ cm$^{-2}$. In a time-resolved analysis of the bursts from SGR 0501+4516, the positive correlation behavior at high fluxes is more significant. Whether the two sources have a similar behavior remains to be seen in the time-resolved analysis of the SGR J1550−5418 bursts. One of the main contributions of the GBM data is providing accurate measurements of the evolution of $E_{\rm peak}$ for short bursts, which is the best hardness indicator for hardness–brightness correlation studies.

For the BB+BB fits, we find average temperatures of ∼5 and ∼14 keV and we show that these temperatures are well correlated. The fluences of the two BB functions are strongly correlated, and the same is true for their emission areas. The emission area of the low-temperature BB is comparable to the neutron star surface area; the hot BB area is much smaller and strongly anti-correlated with its temperature.

A.J.v.d.H. thanks Vicky Kaspi for useful discussions. This publication is part of the GBM/Magnetar Key Project (NASA grant NNH07ZDA001-GLAST, PI: C. Kouveliotou). Y.K. and E.G. acknowledge the support from the Scientific and Technological Research Council of Turkey (TÜBİTAK) through grant 109T755. M.G.B. acknowledges support from NASA through grant NNX10AC59A. S.G. was supported by an appointment to the NASA Postdoctoral Program at the Goddard Space Flight Center, administered by Oak Ridge Associated Universities through a contract with NASA. J.G. is supported by the ERC advanced research grant "GRBs." A.L.W. acknowledges support from an NWO Vidi Grant.

## REFERENCES

Arnaud, K. A. 1996, in ASP Conf. Ser. 101, Astronomical Data Analysis Software and Systems V, ed. G. H. Jacoby & J. Barnes (San Francisco, CA: ASP), 17
Bellm, E., Smith, D. M., & Hurley, K. 2009, GRB Coordinates Network, 8857, 1
Beloborodov, A. M., & Thompson, C. 2007, ApJ, 657, 967
Bernardini, F., Israel, G. L., Stella, L., et al. 2011, A&A, 529, A19
Bissaldi, E., von Kienlin, A., Lichti, G., et al. 2009, Exp. Astron., 24, 47
Camilo, F., Ransom, S. M., Halpern, J. P., et al. 2006, Nature, 442, 892
Camilo, F., Ransom, S. M., Halpern, J. P., & Reynolds, J. 2007, ApJ, 666, L93
Camilo, F., Reynolds, J., Johnston, S., Halpern, J. P., & Ransom, S. M. 2008, ApJ, 679, 681
Chakrabarti, S. K., Mondal, S. K., Sasmal, S., & Bhowmick, D. 2009, GRB Coordinates Network, 8881, 1
Connaughton, V., & Briggs, M. 2009, GRB Coordinates Network, 8835, 1
Cordes, J. M., & Lazio, T. J. W. 2002, arXiv:astro-ph/0207156
Duncan, R. C., & Thompson, C. 1992, ApJ, 392, L9
Esposito, P., Israel, G. L., Zane, S., et al. 2008, MNRAS, 390, L34
Fenimore, E. E., Laros, J. G., & Ulmer, A. 1994, ApJ, 432, 742
Feroci, M., Caliandro, G. A., Massaro, E., Mereghetti, S., & Woods, P. M. 2004, ApJ, 612, 408
Gavriil, F. P., Kaspi, V. M., & Woods, P. M. 2004, ApJ, 607, 959
Gelfand, J. D., & Gaensler, B. M. 2007, ApJ, 667, 1111
Göğüş, E., Kouveliotou, C., Woods, P. M., et al. 2001, ApJ, 558, 228
Göğüş, E., Woods, P. M., Kouveliotou, C., et al. 1999, ApJ, 526, L93
Göğüş, E., Woods, P. M., Kouveliotou, C., et al. 2000, ApJ, 532, L121
Golenetskii, S., Aptekar, R., Mazets, E., et al. 2009a, GRB Coordinates Network, 8851, 1
Golenetskii, S., Aptekar, R., Mazets, E., et al. 2009b, GRB Coordinates Network, 8858, 1
Golenetskii, S., Aptekar, R., Mazets, E., et al. 2009c, GRB Coordinates Network, 8863, 1
Götz, D., Mereghetti, S., Mirabel, I. F., & Hurley, K. 2004, A&A, 417, L45
Gronwall, C., Holland, S. T., Markwardt, C. B., et al. 2009, GRB Coordinates Network, 8833, 1
Guiriec, S., Connaughton, V., Briggs, M. S., et al. 2011, ApJ, 727, L33
Halpern, J. P., Gotthelf, E. V., Reynolds, J., Ransom, S. M., & Camilo, F. 2008, ApJ, 676, 1178
Israel, G. L., Esposito, P., Rea, N., et al. 2010, MNRAS, 408, 1387
Israel, G. L., Romano, P., Mangano, V., et al. 2008, ApJ, 685, 1114
Kaneko, Y., Göğüş, E., Kouveliotou, C., et al. 2010, ApJ, 710, 1335
Kouveliotou, C., Dieters, S., Strohmayer, T., et al. 1998, Nature, 393, 235
Kouveliotou, C., Meegan, C. A., Fishman, G. J., et al. 1993, ApJ, 413, L101

Krimm, H. A., Beardmore, A. P., Burrows, D. N., et al. 2008a, GRB Coordinates Network, 8311, 1
Krimm, H. A., Beardmore, A. P., Gehrels, N., et al. 2008b, GRB Coordinates Network, 8312, 1
Lamb, R. C., & Markert, T. H. 1981, ApJ, 244, 94
Levin, L., Bailes, M., Bates, S., et al. 2010, ApJ, 721, L33
Lin, L., Kouveliotou, C., Baring, M. G., et al. 2011, ApJ, 739, 87
Meegan, C., Lichti, G., Bhat, P. N., et al. 2009, ApJ, 702, 791
Mereghetti, S. 2008, A&AR, 15, 225
Mereghetti, S., Götz, D., von Kienlin, A., et al. 2009a, GRB Coordinates Network, 8841, 1
Mereghetti, S., Götz, D., Weidenspointner, G., et al. 2009b, ApJ, 696, L74
Miller, M. C. 1995, ApJ, 448, L29
Mitrofanov, I. G., Anfimov, D. S., Litvak, M. L., et al. 1999, ApJ, 522, 1069
Nakagawa, Y. E., Yoshida, A., Hurley, K., et al. 2007, PASJ, 59, 653
Olive, J.-F., Hurley, K., Sakamoto, T., et al. 2004, ApJ, 616, 1148
Perna, R., Heyl, J. S., Hernquist, L. E., Juett, A. M., & Chakrabarty, D. 2001, ApJ, 557, 18
Savchenko, V., Beckmann, V., Neronov, A., et al. 2009, GRB Coordinates Network, 8837, 1
Savchenko, V., Neronov, A., Beckmann, V., Produit, N., & Walter, R. 2010, A&A, 510, A77
Scholz, P., & Kaspi, V. M. 2011, ApJ, 739, 94
Starling, R. L. C., van der Horst, A. J., Rol, E., et al. 2008, ApJ, 672, 433
Sugizaki, M., Mitsuda, K., Kaneda, H., et al. 2001, ApJS, 134, 77
Tanaka, Y. T., Raulin, J.-P., Bertoni, F. C. P., et al. 2010, ApJ, 721, L24
Terada, Y., Tashiro, M., Urata, Y., et al. 2009, GRB Coordinates Network, 8845, 1
Thompson, C., & Beloborodov, A. M. 2005, ApJ, 634, 565
Thompson, C., & Duncan, R. C. 1995, MNRAS, 275, 255
Thompson, C., Lyutikov, M., & Kulkarni, S. R. 2002, ApJ, 574, 332
Tiengo, A., Vianello, G., Esposito, P., et al. 2010, ApJ, 710, 227
Ulmer, A. 1994, ApJ, 437, L111
van der Horst, A. J., & Briggs, M. S. 2008, GRB Coordinates Network, 8328, 1
von Kienlin, A., & Briggs, M. S. 2008, GRB Coordinates Network, 8315, 1
von Kienlin, A., & Connaughton, V. 2009, GRB Coordinates Network, 8838, 1
Woods, P. M., Kaspi, V. M., Thompson, C., et al. 2004, ApJ, 605, 378
Woods, P. M., & Thompson, C. 2006, in Compact Stellar X-ray Sources, ed. W. Lewin & M. van der Klis (Cambridge: Cambridge Univ. Press), 547